RSC Advances

PAPER

View Article Online
View Journal | View Issue

Cite this: *RSC Adv.*, 2026, **16**, 26880

Magnetic iron oxide (Fe_3O_4)/carbon nanostructures as cost-effective bifunctional electrodes for energy storage (supercapacitors) and water splitting (OER)

Hani Nasser Abdelhamid, *[a] Faisal Saleh Alshebil[b] and Walid M. Daoush *[b]

Received 14th March 2026
Accepted 4th May 2026

DOI: 10.1039/d6ra02171a

rsc.li/rsc-advances

The development of low-cost, durable, and multifunctional materials for energy storage and conversion is crucial for sustainable energy technologies. This study involved the synthesis of magnetite (Fe_3O_4) nanoparticles and their composites with carbon nanomaterials: graphite (G), carbon fibers (CF), and carbon nanotubes (CNTs), using a straightforward one-pot co-precipitation process facilitated by ultrasonic irradiation. The electrochemical performance was assessed for supercapacitor and oxygen evolution reaction (OER) applications in an alkaline electrolyte. Among the examined materials, Fe_3O_4@CF exhibited the highest specific capacitance of 106 F/g at 1 A/g, with exceptional stability, maintaining 100% efficiency after 5000 cycles. The composites exhibited hybrid charge-storage characteristics, arising from electric double-layer capacitance (EDLC) and Fe^{2+}/Fe^{3+} pseudocapacitance. Moreover, Fe_3O_4 and its composites demonstrated commendable OER activity with low overpotentials of 360–400 mV. The results indicate that Fe_3O_4–carbon nanocomposites, produced using a simple method, are potential bifunctional materials for energy storage and water oxidation applications.

Introduction

Energy has emerged as a paramount concern for contemporary society, driven by rapid population growth, global interconnectivity, and the widespread adoption of electrically powered devices. In this context, energy storage and conversion technologies have become essential components for sustainable development. The rising global demand for durable, high-performance, cost-effective, and environmentally friendly energy storage systems has prompted extensive study into new methods for developing efficient and dependable electrochemical energy conversion devices. Therefore, optimizing energy production and storage systems has emerged as a critical goal.[1,2] Energy storage technologies are essential for improving energy efficiency across multiple industries, especially in transportation systems. Energy storage devices can significantly reduce railway energy consumption.[3] A thorough assessment of the operational characteristics of various energy storage technologies is essential to choose appropriate solutions for certain applications.[4] Supercapacitors (SCs) received significant interest as energy storage devices due to their unique benefits, including extended cycle life and operational safety.[5,6] Extensive research has focused on developing superior electrode materials to enhance the electrochemical performance of supercapacitors. A wide number of materials have been reported, including metal–organic frameworks (MOFs),[7–9] MXenes,[10] nickel–carbon composites,[11] metals/carbon,[12,13] metal oxides,[14–20] metal selenides,[21] phosphorene,[22] nickel cobaltite,[23] and carbonized biomass-derived materials.[24] Carbon-based materials have shown a notable capacity to improve electrical conductivity, structural integrity, and overall electrochemical performance when integrated into composite electrodes.[25–27] Recent advances in bioinspired synthesis have shown that plant extracts can yield highly stable nanoparticle electrodes, *e.g.*, silver nanoparticles[28] and gold nanoparticles.[29] These materials and the new synthesis procedure could reduce costs and offer high efficiency.

Magnetic nanoparticles have garnered considerable attention owing to their ability to enable advanced technological and biomedical applications, driven by their distinctive magnetic, structural, and surface characteristics. Multifunctional magnetic nanoparticles can simultaneously serve therapeutic and diagnostic roles, making them highly appealing for multimodal cancer imaging and treatment.[30,31] Their nanoscale incorporation of magnetic responsiveness facilitates accurate manipulation, targeted administration, and improved imaging contrast. Comprehensive research has validated the efficacy of magnetic nanoparticles across multiple biomedical domains, including nanomedicine, tailored drug delivery systems,[32] cancer diagnosis and therapy,[33] and medical imaging techniques such as magnetic resonance imaging (MRI).[34] These applications can be improved *via* several methods, including

[a]*Department of Chemistry, Faculty of Science, Assiut University, Assiut, 71515, Egypt. E-mail: hany.abdelhamid@aun.edu.eg*

[b]*Department of Chemistry, Faculty of Science, Imam Mohammad Ibn Saud Islamic University (IMSIU), Riyadh, 11623, Saudi Arabia. E-mail: WMDAOUSH@imamu.edu.sa*

the nanoparticles' adjustable surface chemistry, biocompatibility, and responsiveness to external magnetic fields, thereby enhancing targeting efficiency and therapeutic outcomes. In addition to healthcare applications, magnetic nanoparticles have emerged as promising materials for energy-related technologies. Their integration into energy storage devices has been shown to enhance electrochemical performance by improving charge transfer and redox activity.[35,36] Furthermore, the application of external magnetic fields has been shown to enhance energy storage characteristics, providing an additional level of control over electrochemical processes and device performance.[37] Magnetic nanoparticles are often modified or combined with other materials to tailor their physicochemical and functional properties. Polymer surface modification enhances stability, dispersibility, and biocompatibility,[38] whereas hybridization with ZnO/carbon composites[39] and biomass-derived activated carbon[40] enhances electrochemical activity and sustainability. Green synthesis and functionalization methods utilizing natural extracts, such as aegle marmelos pulp extract, have been investigated to enhance environmental compatibility and material efficacy.[41] Moreover, the conjugation of magnetic nanoparticles with carbon nanomaterials, *e.g.*, graphene, carbon nanotubes, and related structures, has been reported to markedly enhance electrical conductivity and surface area.[42–44] Moreover, conjugated polymers have been used to enhance electrical properties and structural flexibility, thereby expanding the utility of magnetic nanoparticle-based composites.[45,46]

Hydrogen production has been extensively investigated using diverse methodologies, including chemical processes,[47] photocatalysis,[48,49] and electrocatalysis.[50] Water electrolysis is notably appealing for its high hydrogen production rate, reliance on renewable energy sources, and use of water as a plentiful, cost-effective feedstock. Notwithstanding these benefits, developing economical, resilient, and effective electrocatalysts for water splitting remains a significant challenge, particularly for the oxygen evolution reaction (OER). The OER is recognized as the rate-limiting, kinetically slow stage in water electrolysis.[51–53] As a result, much research has focused on developing improved OER electrocatalysts, particularly those that utilize magnetic nanoparticles.[54–57] Iron oxide (Fe_3O_4) nanoparticles were reported as a single-atom catalyst,[58] Fe_3O_4@N- doped carbon (NC)/reduced graphene oxide (Fe_3O_4@NC/RGO),[59] Fe_3O_4@NiFe-LDH/$MnCO_3$,[60] Co_3Fe_7/Fe_3O_4,[61] Ir-black@Fe_3O_4,[62] and Fe_3O_4@$CoFe_2O_4$.[63] Despite notable advancements, additional research is needed to improve catalytic efficiency by minimizing critical electrochemical parameters, particularly overpotential, to facilitate the development of viable, sustainable hydrogen production systems.

Taking into account the previous points, this study discusses magnetite (Fe_3O_4) nanoparticles coupled with carbon-based nanomaterials, including carbon fibers (CF), graphite (G), and carbon nanotubes (CNTs). The Fe_3O_4/carbon nanocomposites were prepared *via* a simple one-pot co-precipitation process, thereby facilitating homogeneous integration of the magnetic phase into the conductive carbon matrix. The produced materials were comprehensively evaluated for their structural, morphological, and compositional features using X-ray diffraction (XRD), scanning electron microscopy (SEM), transmission electron microscopy (TEM), energy-dispersive X-ray spectroscopy (EDX), and Fourier transform infrared (FT-IR) spectroscopy. The complementary procedures validated the effective synthesis of magnetite and its uniform distribution inside the carbon matrices. The synthesized nanocomposites were subsequently used as electrode materials for supercapacitor applications. Cyclic voltammetry (CV) and galvanostatic charge–discharge (GCD) measurements were used to evaluate the capacitive behavior, charge-storage capacity, and rate performance.

Experimental section

Materials and methods

Iron(III) chloride hexahydrate ($FeCl_3 \cdot 6H_2O$) was provided by WinLab limited Co, and iron(II) sulfate heptahydrate ($FeSO_4 \cdot 7H_2O$) was purchased from LOBA Chemie (India). Aqueous ammonia solution (NH_4OH), was purchased from Sigma-Aldrich (France), serving as the precipitating agent and pH regulator. Distilled water (H_2O) was used as the reaction medium and washing solvent. Multiwall carbon nanotubes (MWCNTs) of a grade of 10–50 μm length and 15–10 nm diameter with a BET surface area of about 200 m/g^2 were supplied from Iljin Nanotech Co., Ltd. Graphite (G) powder of $10 \sim 50$ μm particle size was provided from Sebersdorf Institute of Technology, Austria. Carbon fibers (CFs) bobine PAN-Type (Polyacrylonitrile Fiber) of ~6.7 μm diameter were purchased from Mitsubishi Chemicals Co., Ltd. Approximately 6 cm of carbon fibers were cut before using them in the current experiments.

Synthesis of magnetite nanoparticles

Magnetite (Fe_3O_4) nanoparticles were produced using a co-precipitation process facilitated by ultrasonic irradiation. In a 50 mL beaker, 1.95 g of $FeCl_3$ and 1.08 g of $FeSO_4$ were solubilized in 15 mL of distilled water. The solution was agitated under ultrasonic irradiation (40 kHz) for 15 minutes and then heated to 60 °C. Ten milliliters of ammonia solution (28–30%) were added dropwise over three minutes while maintaining a temperature of 60 °C and ultrasonic irradiation at 40 kHz. The pH value was modified to 12.5. The process concluded in 15 minutes, during which the fluid transitioned from brown to black, signifying the synthesis of magnetite nanoparticles. The resultant precipitate was repeatedly rinsed with distilled water, collected *via* centrifugation at 4000 rpm for 1 minute, and subsequently dried at 100 °C for 1 hour.

Synthesis of Fe_3O_4@G nanocomposites

Fe_3O_4@G nanocomposites were fabricated *via* an *in situ* co-precipitation method. In a 50 mL beaker, 1.68 g of $FeCl_3$ and 1.04 g of $FeSO_4$ were solubilized in 15 mL of distilled water with magnetic stirring at 350 rpm for 15 minutes. The solution was subsequently exposed to ultrasonic irradiation (40 kHz) for an

additional 15 minutes and heated to 60 °C. An exact quantity of graphite powder (0.098 g) was added to the solution, which was then sonicated at 40 kHz for 15 minutes to achieve uniform dispersion. Subsequently, 10 mL of ammonia solution was added incrementally over 3 minutes while maintaining the temperature at 60 °C and the pH at 12.5 under ultrasonic irradiation.

The resultant composite was washed, centrifuged at 4000 rpm for 1 minute, and subsequently dried at 100 °C for 1 hour. The product was preserved for subsequent analysis and characterization.

Synthesis of Fe_3O_4@CF nanocomposite

Fe_3O_4@CF nanocomposites were prepared by co-precipitation. In a 50 mL beaker, 1.95 g of $FeCl_3 \cdot 6H_2O$ and 1.08 g of $FeSO_4 \cdot 7H_2O$ were solubilized in 15 mL of distilled water by magnetic stirring at 350 rpm for 15 minutes, followed by ultrasonic irradiation at 40 kHz for 15 minutes, and then heating to 60 °C. Carbon fibers (0.079 g) were added to the solution, and the reaction mixture was heated to 60 °C. Ammonia solution (10 mL) was added incrementally over 3 minutes to reach a pH of 12.5. Following the process, magnetite-coated carbon fibers were produced. The resultant product was washed with distilled water, then dried at 100 °C for 1 hour.

Synthesis of Fe_3O_4@CNT nanocomposites

Fe_3O_4@CNT nanocomposites were fabricated using an ultrasonic-assisted co-precipitation technique. In a 50 mL beaker, 1.68 g of $FeCl_3$ and 1.04 g of $FeSO_4$ were dissolved in 15 mL of distilled water using magnetic stirring at 350 rpm for 15 min, followed by ultrasonic irradiation (40 kHz) for an additional 15 min. The solution was increased to 60 °C. A certain amount of carbon nanotubes (9.1 mg) was added to the solution and sonicated at 40 kHz for 15 minutes to achieve uniform dispersion. Ammonia solution (10 mL) was then added dropwise over 3 min to adjust the pH to 12.5 while maintaining ultrasonic irradiation and temperature.

The resulting nanocomposite was washed several times, centrifuged at 4000 rpm for 1 min, and dried at 100 °C for 1 h. The dried powder was preserved for subsequent characterization and analysis.

Characterization

The particle size, morphology, and surface features of the synthesized powders were evaluated using SEM equipped with an EDX detector (JEOL JSM-7600 F). Materials were sputtered with platinum to improve contrast of SEM images. Crystalline phase identification was carried out using XRD analysis performed on a Bruker D8 Discover diffractometer. In addition, TEM analysis was performed using a JEM-2100F (JEOL) operated at 300 kV to further investigate nanoscale structure and particle morphology. FT-IR spectra were collected using IRTracer-100 (Shimadzu).

Electrochemical measurements

Electrochemical performance evaluations were carried out at ambient temperature using a conventional three-electrode configuration on a Studio 6 electrochemical workstation (Corrtest®, CS150M, Wuhan, China). CV measurements were conducted within a potential window of 0.2–0.6 V at scan rates ranging from 1 to 200 mV/s. GCD measurements were performed at current densities of 1, 3, 5, and 10 A/g. In the three-electrode system, the active material/nickel foam is used as the working electrode, while a platinum wire and a saturated Ag/AgCl electrode serve as the counter and reference electrodes, respectively. A 6 M KOH aqueous solution was employed as the electrolyte. The electrode slurry was prepared by dispersing the active material, carbon black, and poly(vinylidene fluoride) in dimethylformamide and ultrasonically treating for 1 h to ensure homogeneous dispersion.

The specific capacitance from GCD is calculated using eqn (1):

$$\text{Specific capacitance}(\text{F/g}) = \frac{\text{discharge current}(A)\cdot\text{discharge time }(s)}{\text{mass of active material}(g)\cdot\text{potential window}(V)} \quad (1)$$

The relationship between current and scan rate is determined using eqn (2):

$$\log(i) = \log(a) + b\log(\nu) \quad (2)$$

where: i, ν, b represent peak current (A), scan rate, and slope of $\log(i)$ *vs.* $\log(\nu)$.

Dunn Method (capacitive *vs.* diffusion contribution) is evaluated using eqn 3

$$\frac{i(V)}{\nu^{1/2}} = k_1\nu^{1/2} + k_2 \quad (3)$$

where: $k_1\nu$ and $k_2\nu^{1/2}$ represent the capacitive (surface-controlled) contribution and the diffusion-controlled contribution, eqn (4) and (5).

$$\text{Capacitive contribution} = \frac{k_1\nu}{i(V)} \times 100 \quad (4)$$

$$\text{Diffusion contribution} = \frac{k_2\nu^{1/2}}{i(V)} \times 100 \quad (5)$$

The oxygen evolution reaction (OER) was assessed by linear sweep voltammetry (LSV) in a three-electrode setup, as previously detailed. Measurements were performed within a potential range of −1 to +1 V relative to an Ag/AgCl reference electrode.

Results and discussion

Materials characterization

Fig. 1 represents the schematic representation of materials synthesis. Magnetite (Fe_3O_4) nanoparticles and their carbon-

based nanocomposites were produced by a simple ultrasonic-assisted co-precipitation method. The approach facilitated the synthesis of pure Fe_3O_4 nanoparticles and their conjugation with three different carbon nanomaterials, such as graphite, carbon fibers, and carbon nanotubes. The alkaline reaction conditions facilitated rapid nucleation and growth of magnetite, as indicated by the distinctive color change during synthesis. The *in situ* integration of carbon materials during co-precipitation enabled close interfacial contact between Fe_3O_4 nanoparticles and the carbon substrates, resulting in uniformly dispersed magnetite coatings or magnetite nanoparticles attached to the substrates. Ultrasonic irradiation significantly enhanced precursor dispersion, mitigated particle aggregation, and improved the homogeneity of the resultant composites. Post-synthesis washing and heat treatment produced stable, phase-pure materials appropriate for subsequent structural, morphological, and electrochemical characterization. The materials were characterized using XRD (Fig. 2a), SEM images (Fig. 2b and c), FT-IR (Fig. 2d), EDX analysis, and a TEM image (Fig. 3–5).

Fig. 2a displays the XRD patterns of Fe_3O_4 and its carbon-based composites. The XRD pattern of Fe_3O_4 displays distinct diffraction peaks at 2θ values of 30.09°, 35.50°, 56.98°, and 62.56°, corresponding to the (220), (311), (511), and (440), respectively, thereby affirming the establishment of a spinel structure of magnetite (JCPDS No. 19-0629). In the Fe_3O_4@G composite, an extra diffraction peak is observed at 26.5°, which corresponds to the (002) plane of graphitic carbon, hence validating the integration of graphite into the composite. The Fe_3O_4@CF composite exhibits a broad diffraction peak at around 12.76°, which is attributed to the carbon fibers (Fig. 2a). The extensive nature of this peak indicates the primarily amorphous or inadequately graphitized structure of the carbon fibers, aligning with other findings.

The Fe_3O_4@CNTs composite shows the distinctive magnetite diffraction peaks, indicating that the crystalline structure of Fe_3O_4 is preserved after modification (Fig. 2a). A strong diffraction pattern detected at a Bragg angle of $2\theta = 32.41°$ indicates the existence of magnetite nanoparticles (Fig. 2a). The lack of discernible CNT-related diffraction peaks may be due to their low concentration or to interference with the magnetite reflections. Data analysis confirms the effective synthesis of Fe_3O_4 and its carbon-based nanocomposites, with the carbon components exhibiting distinct diffraction patterns while preserving the magnetite phase's crystalline structure (Fig. 2a).

The morphology and particle size of Fe_3O_4 nanoparticles were evaluated *via* SEM (Fig. 2b). The SEM image demonstrates that the Fe_3O_4 nanoparticles generally exhibit a spherical morphology, with particle sizes ranging from 25 to 50 nm, indicating a relatively homogeneous nanoscale distribution. EDX was conducted to analyze the elemental composition of the produced Fe_3O_4 nanoparticles (Fig. 2c). Upon removing contributions from sputtered platinum, applied to the samples to improve the image's contrast, and from carbon from sample processing, the EDX spectrum verifies the presence of solely iron and oxygen. This outcome illustrates the high chemical purity of the synthesized Fe_3O_4 nanoparticles and the lack of identifiable contaminants.

Fig. 2d displays the FT-IR spectra of the synthesized samples, specifically Fe_3O_4 and its composites. The spectra display analogous profiles across all materials, indicating the presence of identical functional groups and suggesting that the addition of carbon-based components does not substantially alter the intrinsic chemical structure of Fe_3O_4. Distinct absorption bands are observed at around 570 cm^{-1} and 656 cm^{-1}, which can be ascribed to Fe–O stretching vibrations, thereby affirming the emergence of the Fe_3O_4 phase. Supplementary bands are observed at 1130 cm^{-1} and 1388 cm^{-1}, commonly linked to C–O/C–N and C–H vibrations. Bands are observed at around

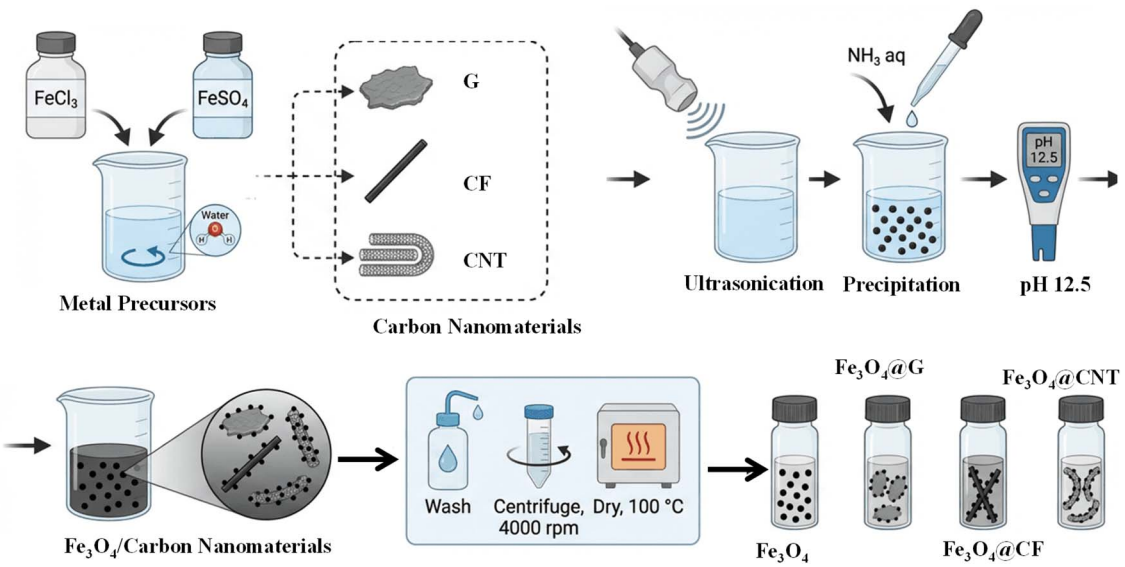

Fig. 1 Systematic representation for the synthesis of Fe_3O_4 and its composites with carbon fiber, graphite, and carbon nanotubes.

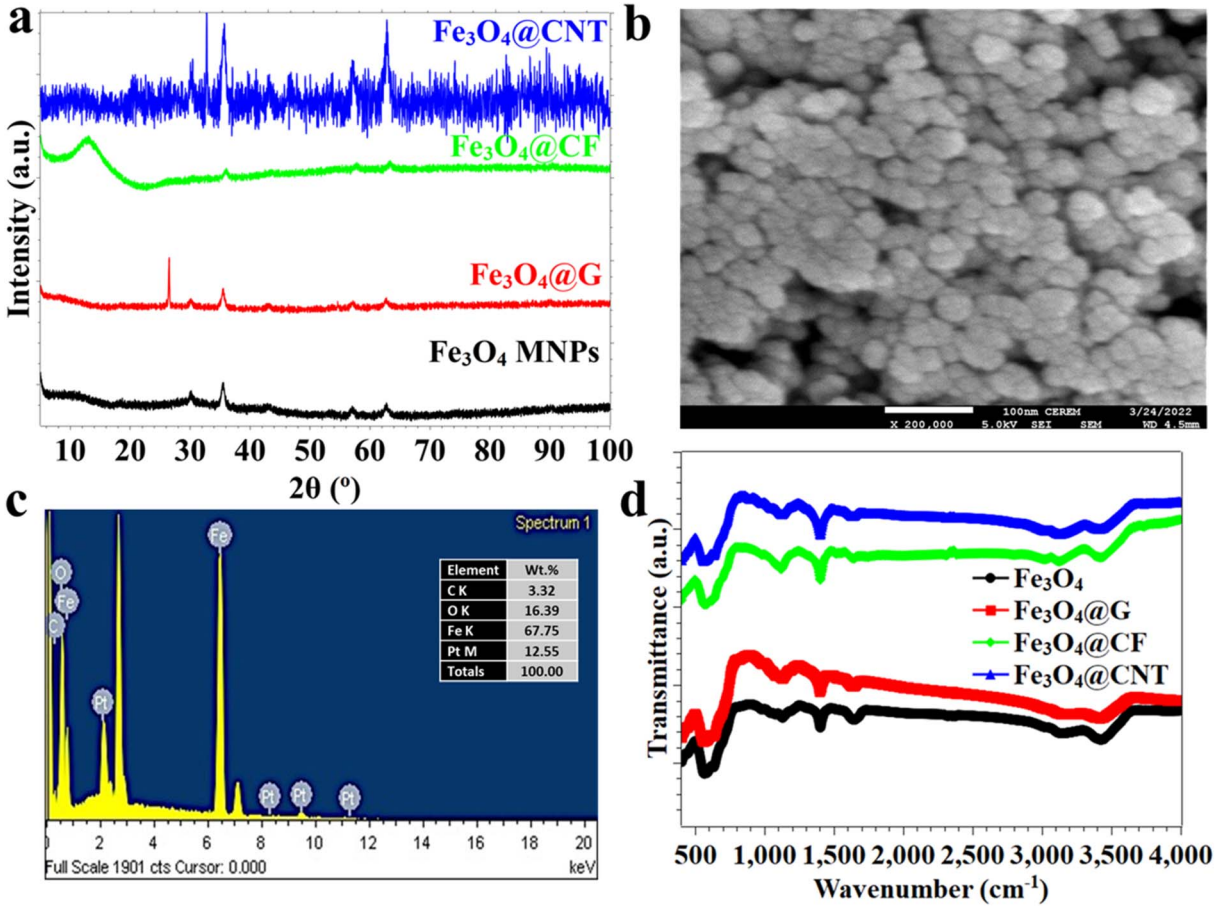

Fig. 2 Characterization of Fe_3O_4 and its composites using (a) XRD, (b) SEM image, (c) EDX analysis for pristine Fe_3O_4, and (d) FT-IR.

570 cm^{-1} and 656 cm^{-1}, which can be ascribed to Fe–O stretching vibrations, thereby verifying the existence of surface functional groups connected with carbon constituents or residual organic entities. The band at approximately 1630 cm^{-1} is associated with bending vibrations of adsorbed water molecules or with C=C stretching. The bands at 3450 cm^{-1} are ascribed to O–H stretching vibrations, signifying the presence of hydroxyl groups or absorbed moisture on the material's surface. The FT-IR results validate the effective synthesis of Fe_3O_4 and its composites.

Fig. 3a–c display the SEM images of graphite and the Fe_3O_4@G nanocomposite, whereas Fig. 3d illustrates the related EDX analysis. The SEM image of graphite displays a distinctive layered architecture with particle sizes in the micrometer scale (Fig. 3a). SEM images of Fe_3O_4@G demonstrate that the Fe_3O_4 is dispersed on the graphite surface, with no significant changes in the particle size of Fe_3O_4 compared to the pristine nanoparticles (Fig. 3b and c). This observation indicates that the composite preparation process does not promote particle aggregation. The EDX spectrum of the Fe_3O_4@G composite verifies the presence of iron, oxygen, and carbon, with no detectable impurities, indicating the high purity of the synthesized composite and the successful conjugation of Fe_3O_4 with graphite (Fig. 3d).

Fig. 4a–c display the SEM images of CF and the Fe_3O_4@CF nanocomposite, whereas Fig. 4d illustrates the associated EDX analysis. The SEM image of CF displays distinct fibrous structures with an average diameter of about 4.5 μm (Fig. 4a). Post-composite formation, the SEM images of Fe_3O_4@CF illustrate the incorporation of Fe_3O_4 nanoparticles into the CF surface (Fig. 4b and c). The magnetite nanoparticles are evenly dispersed on the fiber surface, demonstrating effective interaction between Fe_3O_4 and CF without considerable aggregation. The EDX spectrum of the Fe_3O_4@CF composite corroborates the presence of iron, oxygen, and carbon, hence affirming the excellent purity of the synthesized composite and the lack of observable impurity phases (Fig. 4d).

Fig. 5 illustrates the morphological and chemical analysis of CNTs and the Fe_3O_4@CNT nanocomposite. Fig. 5a and b illustrate the TEM and SEM images of CNTs, respectively. The TEM image shows the distinctive tubular morphology of CNTs, with an average diameter of approximately 12.5 nm (Fig. 5a), consistent with the SEM image (Fig. 5b). The SEM image of the Fe_3O_4@CNT composite shows effective decoration of the CNT surfaces with Fe_3O_4 nanoparticles, while preserving the original magnetite particle size, indicating low aggregation during composite synthesis (Fig. 5c). The EDX spectrum corroborates the presence of iron, oxygen, and carbon, with no detectable

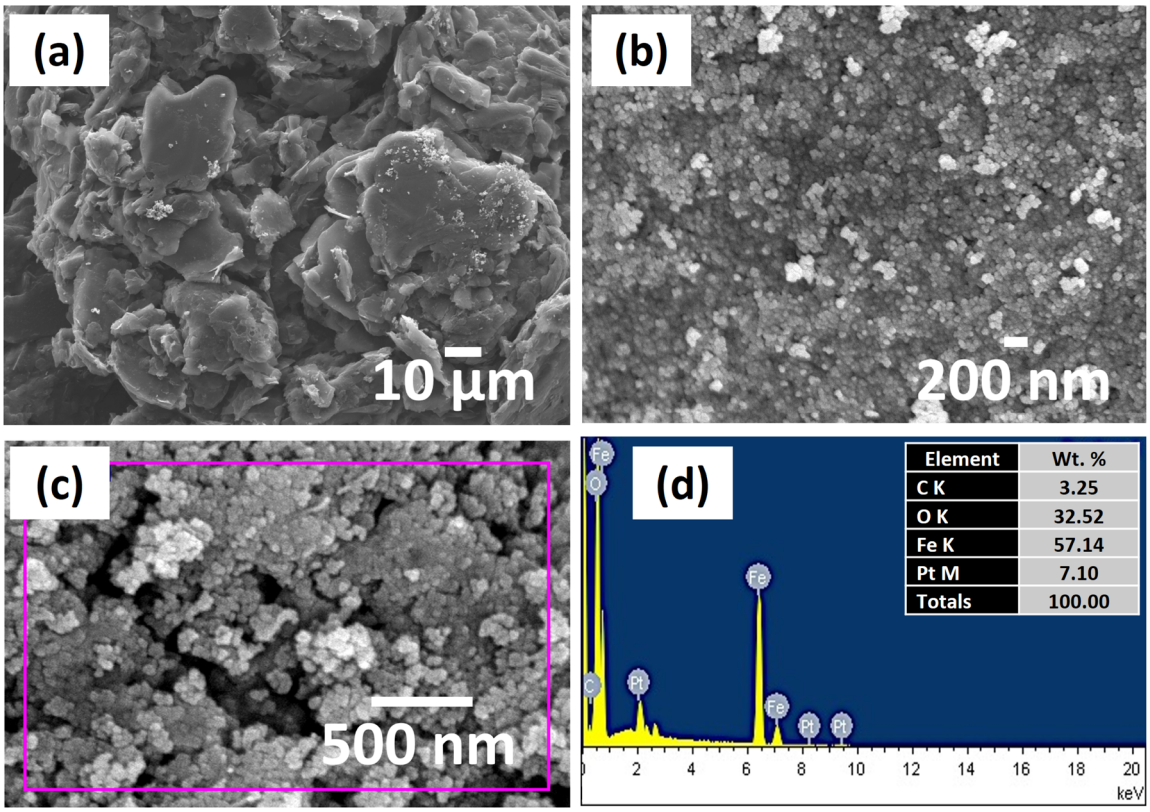

Fig. 3 (a–c) SEM images for (a) graphite and (b and c) Fe_3O_4@G and (d) EDX analysis.

impurities, thereby affirming the exceptional purity of the produced Fe_3O_4@CNT composite (Fig. 5d).

Electrochemical applications

Fig. 6 illustrates the CV curves for Fe_3O_4 (Fig. 6a), Fe_3O_4@G (Fig. 6b), Fe_3O_4@CF (Fig. 6c), and Fe_3O_4@CNTs (Fig. 6d), obtained at scan rates between 1 and 200 mV/s. For all samples, the current response and the area under the CV curves increase with increasing scan rate, indicating improved charge storage behavior and excellent rate capacity. The CV curves of virgin Fe_3O_4 exhibit distinct redox peaks at around 0.46 V (oxidation) and 0.34 V (reduction), corresponding to the reversible Fe^{2+}/Fe^{3+} redox processes (Fig. 6a). Significant changes in the redox peak positions are seen upon composite production. The Fe_3O_4@G composite (Fig. 6b) displays oxidation and reduction peaks at 0.44 V and 0.31 V, respectively, whereas Fe_3O_4@CF (Fig. 6c) presents peaks at 0.43 V and 0.29 V. The Fe_3O_4@CNTs composite exhibits redox maxima at 0.43 V and 0.313 V (Fig. 6d). The systematic variations in redox potentials compared to pristine Fe_3O_4 suggest significant interfacial interactions between Fe_3O_4 nanoparticles and various carbon nanomaterials (G, CF, and CNTs). These interactions enhance charge-transfer kinetics and improve the performance of the Fe_3O_4-based composites.

The charge–discharge characteristics of pristine Fe_3O_4 and its carbon-based composites were examined by GCD tests, as seen in Fig. 7. The measurements were conducted at 1, 3, 5, and 10 A/g. Fig. 7a–d illustrate the GCD curves for Fe_3O_4, Fe_3O_4@G, Fe_3O_4@CF, and Fe_3O_4@CNTs, respectively. The GCD profiles reveal distinct charge–discharge characteristics for Fe_3O_4 and its composites, highlighting the effect of carbon nanoparticles on magnetite's electrochemical properties. Pristine Fe_3O_4 exhibits charge–discharge curves with voltage plateaus, indicating pseudocapacitive behavior arising from reversible Fe^{2+}/Fe^{3+} redox processes. This pseudocapacitive behavior is retained upon combining Fe_3O_4 with carbon materials, including graphite, carbon fibers, and CNTs. The Fe_3O_4-based composites exhibit hybrid charge-storage characteristics, integrating pseudocapacitance from Fe_3O_4 with electric double-layer capacitance (EDLC). This synergistic effect improves the charge transport and promotes overall electrochemical performance. Pristine Fe_3O_4 and Fe_3O_4@CNTs demonstrate shorter discharge durations than Fe_3O_4@CF and Fe_3O_4@G, indicating variations in ion diffusion kinetics and interfacial charge storage processes among the composites.

Fig. 8 depicts the specific capacitance as a function of current density (Fig. 8a) and electrode material (Fig. 8b) for Fe_3O_4 and its carbon-based composites. Fig. 8a shows that the specific capacitance decreases as the current density increases from 1 to 10 A/g, a characteristic behavior of supercapacitor electrodes, attributable to restricted ion diffusion and decreasing active-site utilization at high charge–discharge rates. At a low current density of 1 A/g, Fe_3O_4@CF has the largest specific capacitance of 106 F/g, surpassing pristine Fe_3O_4 at 35.5

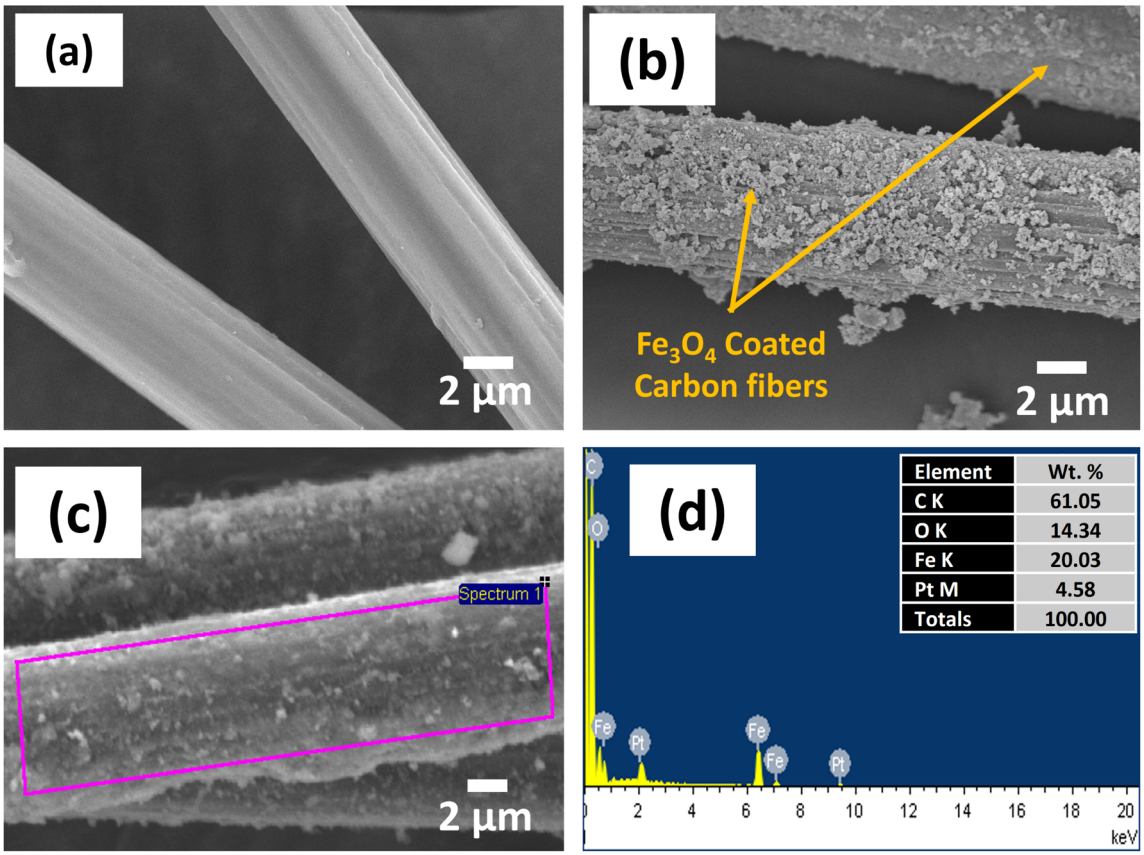

Fig. 4 (a–c) SEM images for (a) carbon fibers and (b and c) Fe_3O_4@CF and (d) EDX analysis.

F/g, Fe_3O_4@G at 49.5 F/g, and Fe_3O_4@CNTs at 19.2 F/g, as illustrated in Fig. 8b. The improved performance can be attributed to the synergistic interaction between Fe_3O_4 pseudocapacitance and the conductive, fibrous carbon framework, which promotes efficient electron transport and ion diffusion. As current density increases, Fe_3O_4@CF consistently exhibits superior capacitance values compared to other materials, preserving 43.3, 27.1, and 12.5 F/g at 3, 5, and 10 A/g, respectively. In contrast, Fe_3O_4 and Fe_3O_4@G exhibit reasonable capacitance retention, whereas Fe_3O_4@CNTs shows the lowest specific capacitance across all current densities. Among the investigated composites, Fe_3O_4@CF exhibits the most advantageous charge-storage characteristics, underscoring the benefits of CF incorporation in enhancing capacitance and rate performance through improved electrical conductivity and structural accessibility.

The cycling stability of Fe_3O_4@CF was assessed for 5000 charge–discharge cycles at a current density of 10 A/g, as depicted in Fig. 8c. The results reveal small variation in specific capacitance during the cycling test, indicating superior electrochemical stability. The consistent performance validates the excellent recyclability of the Fe_3O_4@CF electrode and underscores its structural integrity and prolonged durability across numerous charge–discharge cycles. Carbon-based nanomaterials have been shown to effectively mitigate oxidative stress and enhance material resilience,[64] consistent with the improved cycling stability observed in our Fe_3O_4@CF composite.

The energy storage mechanism of the synthesized electrodes was examined using b-value analysis and the Dunn technique, as illustrated in Fig. 8d and 9. The determined b-values for Fe_3O_4, Fe_3O_4@G, Fe_3O_4@CF, and Fe_3O_4@CNT are 1.0, 0.71, 0.76, and 0.71, respectively. A *b*-value near 1 signifies primarily surface-controlled capacitive (pseudocapacitive) activity, whereas values ranging from 0.5 to 1 indicate a mixture of capacitive and diffusion-controlled mechanisms. Consequently, Fe_3O_4 exhibits near-optimal capacitive behavior, whereas the composite materials exhibit hybrid charge-storage mechanisms with considerable pseudocapacitive contributions. Additional kinetic analysis was conducted utilizing the correlations between log(i) and log(ν) and sqrt(ν) *vs.* $i(V)$/sqrt(ν), as illustrated in Fig. 9. The linear regression of log(i) against log(ν) exhibits remarkable correlation, with regression coefficients (R^2) of 1.000, 0.998, 0.998, and 0.997, alongside minimal Root Mean Squared Error (RMSE) values of 0.000, 0.026, 0.026, and 0.030 for Fe_3O_4, Fe_3O_4@G, Fe_3O_4@CF, and Fe_3O_4@CNT, respectively. These findings validate the robustness of the kinetic model and the significant correlation between current and scan rate. Likewise, the sqrt(ν) *vs.* $i(V)$/sqrt(ν) graphs demonstrate strong linearity for the composite materials, with R^2 values of 0.976, 0.985, 0.959, and 0.955, accompanied by low RMSE values, so

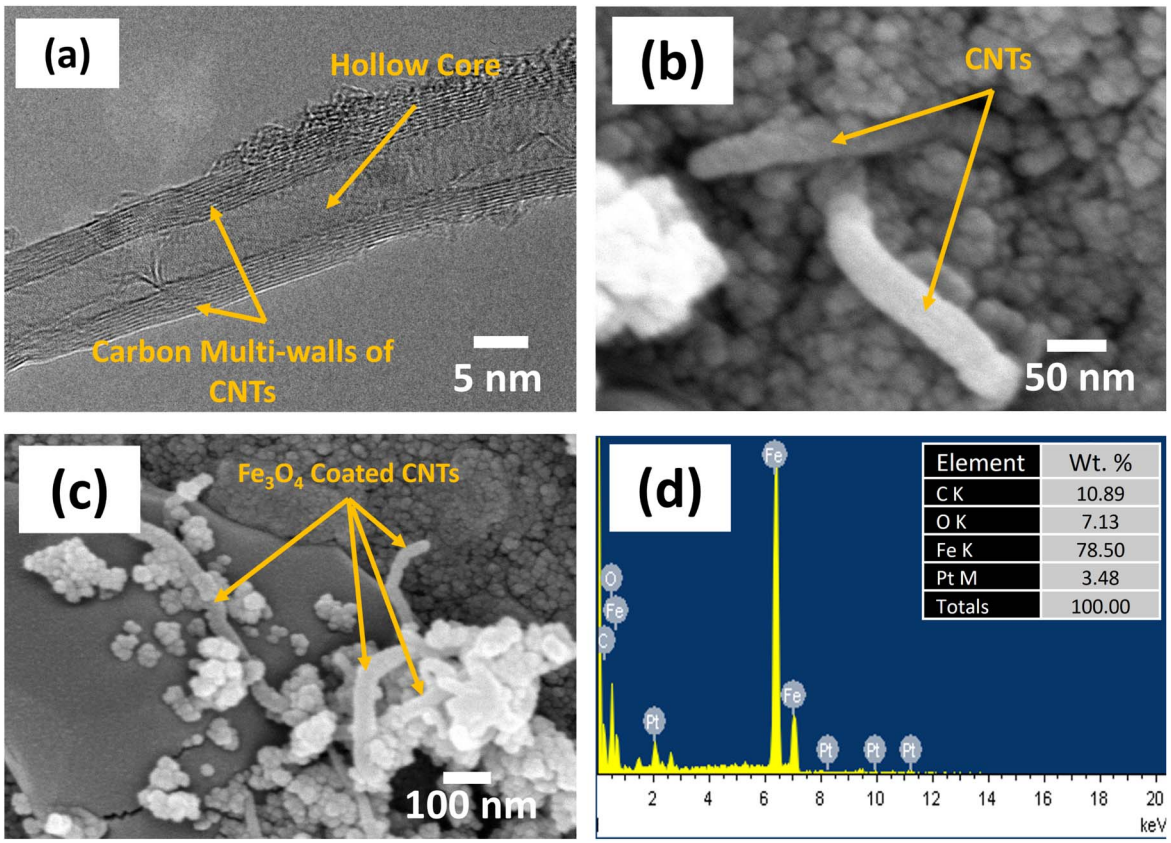

Fig. 5 (a) TEM and (b) SEM image of CNT, (c) SEM images for Fe_3O_4@CNTs, and (d) EDX analysis.

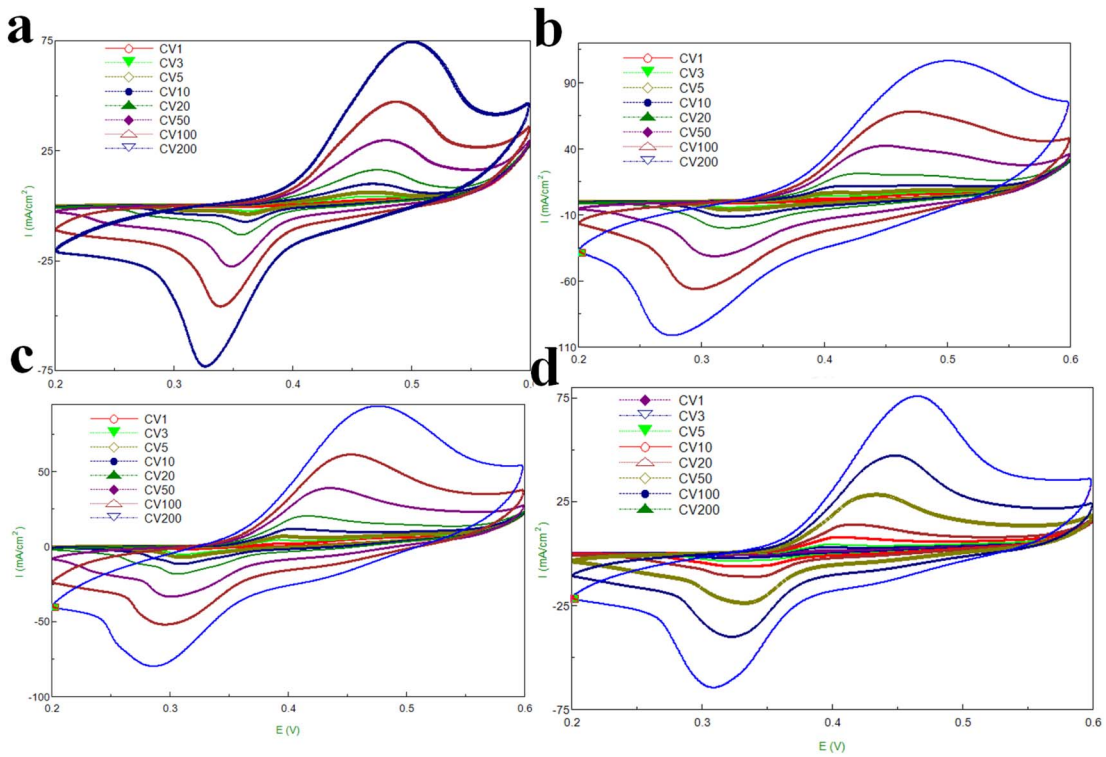

Fig. 6 CV curves for (a) Fe_3O_4, (b) Fe_3O_4@G, (c) Fe_3O_4@CF, and (d) Fe_3O_4@CNTs.

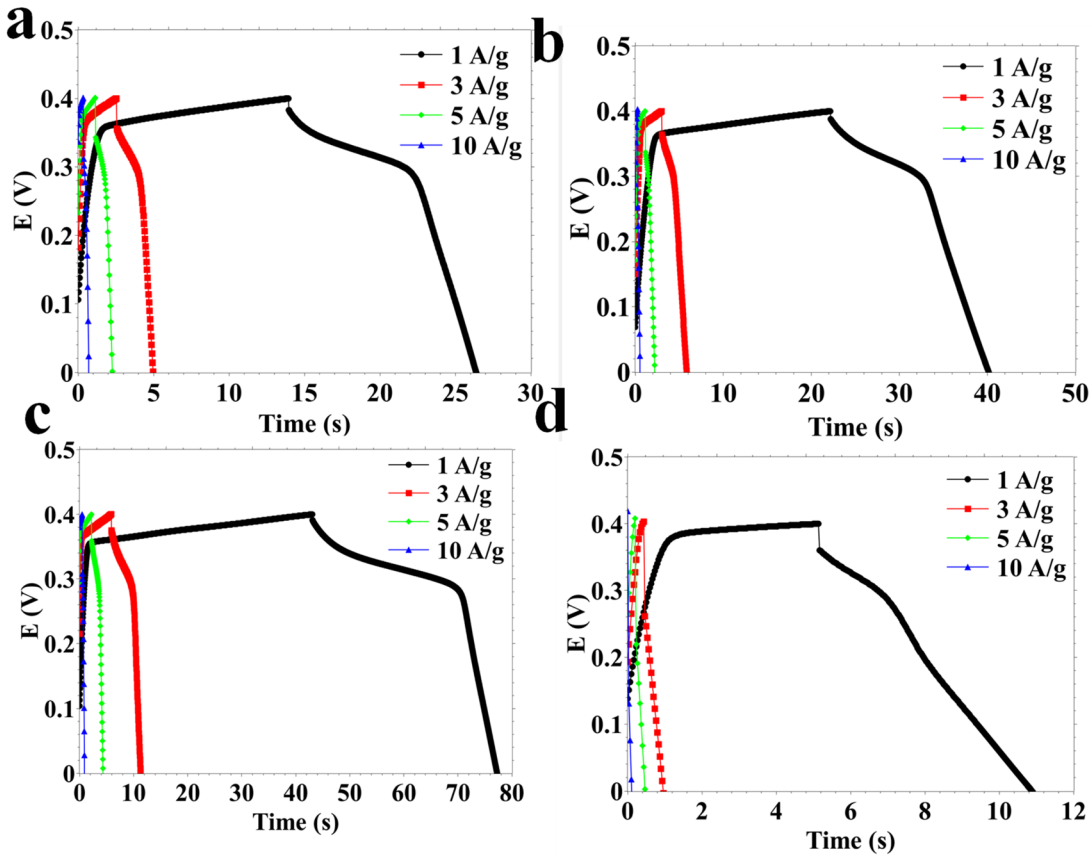

Fig. 7 GCD curves for (a) Fe_3O_4, (b) Fe_3O_4@G, (c) Fe_3O_4@CF, and (d) Fe_3O_4@CNTs.

reinforcing the credibility of the diffusion–capacitive separation analysis.

The Dunn technique was subsequently employed to quantify the relative contributions of capacitive (surface-controlled) and diffusion-controlled processes at various scan rates. Fig. 9 illustrates that the contribution of each mechanism varies with the material and the scan rate. Pure Fe_3O_4 and Fe_3O_4@G exhibit predominant capacitive behavior, characterized by a significant surface-controlled contribution and negligible diffusion impact. Conversely, Fe_3O_4@CF and Fe_3O_4@CNT exhibit a high dependence on scan rate, with the capacitive contribution increasing as the scan rate increases, while the diffusion-controlled contribution decreasing. At a low scan rate of 1 mV/s, the capacitive contributions are approximately 99.5%, 91.9%, 23%, and 30% for Fe_3O_4, Fe_3O_4@G, Fe_3O_4@CF, and Fe_3O_4@CNT, respectively, with the lower contribution attributed to diffusion-controlled processes. At high scan rates, the capacitive contribution is high, especially in composite materials, owing to accelerated surface reactions and restricted ion diffusion. These results indicate that the incorporation of carbon nanomaterials affects the charge storage mechanism by enhancing capacitive contributions and improving electrochemical kinetics, particularly at high scan rates.

Fig. 8 and Table 1 illustrate the electrochemical superiority of Fe_3O_4@CF in comparison to pristine Fe_3O_4 and other Fe_3O_4-based composites. In this study, Fe_3O_4@CF demonstrates the highest specific capacitance of 106 F/g at 1 A/g, nearly threefold that of pristine Fe_3O_4 (35.5 F/g) and more than double that of Fe_3O_4@G (49.5 F/g). This improvement is due to the efficient incorporation of Fe_3O_4 nanoparticles into the conductive carbon fiber matrix, which enhances electrical conductivity, promotes ion transport, and optimizes the use of electrochemically active sites. A comparison with previously reported magnetic nanoparticles further underscores the competitive efficacy of Fe_3O_4@CF. An environmentally sustainable anode material composed of activated carbon from Abelmoschus esculentus seed biomass (AE-AC) doped with Fe_3O_4 nanoparticles exhibited a high specific capacitance of 205.86 F/g at a low current density of 0.05 A/g.[40] This value exceeds that of Fe_3O_4@CF, however it was achieved at a far lower current density and incorporated chemical activation processes along with biomass-derived precursors. Conversely, the current Fe_3O_4@CF composite was synthesized *via* a straightforward one-pot co-precipitation method and exhibited significant capacitance at a higher and more practical current density of 1 A/g. In a similar manner, *in situ* carbon-coated Fe_3O_4 (ISCC-Fe_3O_4) produced with glucose as a carbon precursor exhibited a specific capacitance of 150 F/g at 1.5 A/g in a Na_2SO_4 electrolyte.[42] The improved performance of ISCC-Fe_3O_4 was ascribed to its multi-porous architecture and uniform carbon coating developed at a high carbonization temperature (1200 °C). While ISCC-Fe_3O_4 exhibits superior capacitance, its synthesis requires

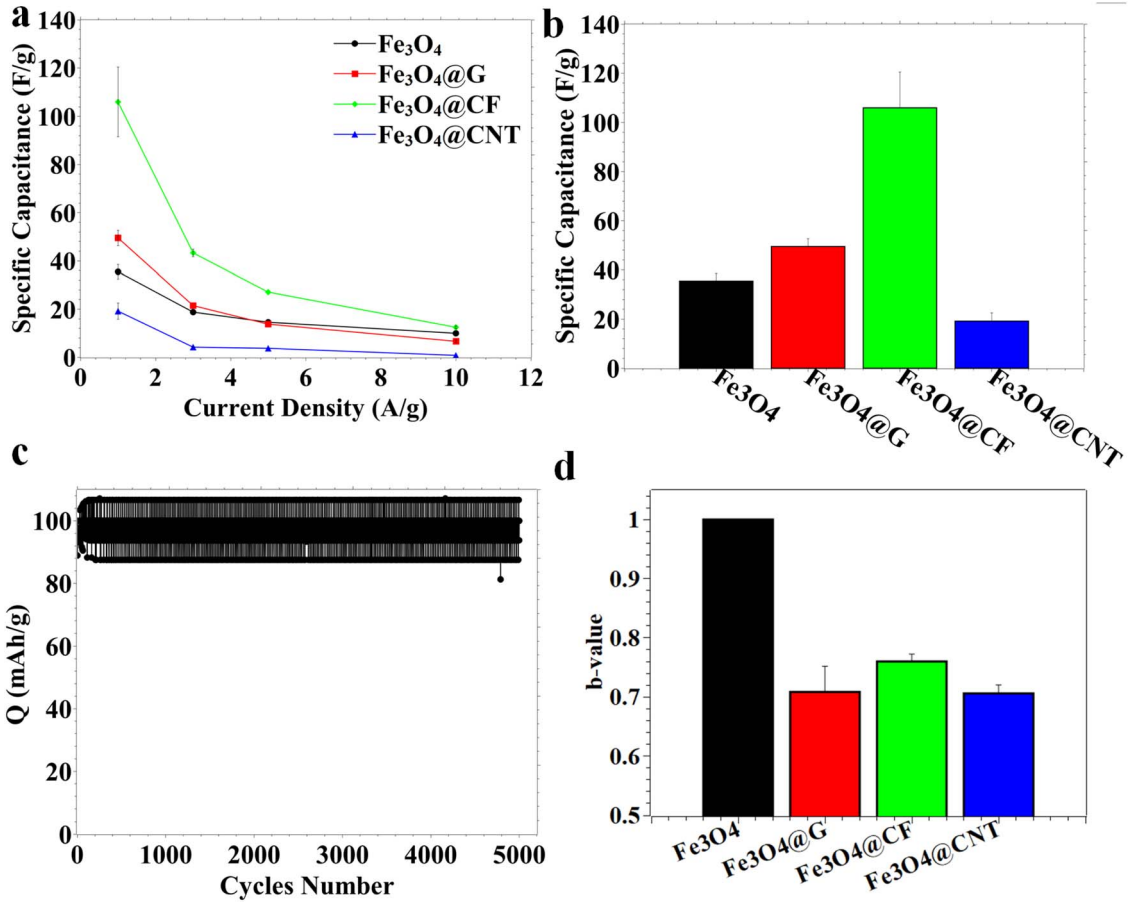

Fig. 8 (a and b) Specific capacitance *vs.* (a) current densities and (b) different materials, (c) recycling of Fe_3O_4@CF at a current density of 10 A/g, and (d) *b*-value.

high-temperature processing and polymer additives, whereas Fe_3O_4@CF achieves commendable performance *via* a simpler, energy-efficient synthesis method. Complex nanostructured systems, such as Fe_3O_4 on reduced graphene oxide (Fe_3O_4@rGO), have demonstrated remarkably high capacitance values of 326 F/g, accompanied by high energy density.[43] Similarly, carbon-coated Fe_3O_4 hybrid nanoparticles produced by electrospraying and vapor-deposition polymerization demonstrated a capacitance of up to 455 F/g.[45] Although these systems exceed Fe_3O_4@CF in absolute capacitance, they depend on complex fabrication methods, expensive precursors, and multistage processing. In contrast, Fe_3O_4@CF offers an advantageous balance among electrochemical performance, simple synthesis procedures, and material cost. The carbon fiber matrix enhances electronic conductivity, provides mechanical stability, and facilitates efficient access to the electrolyte, thereby improving the pseudocapacitive behavior of the Fe^{2+}/Fe^{3+} redox system. The specific capacitance of 106 F/g at 1 A/g highlights the viability of Fe_3O_4@CF as a scalable, cost-effective electrode material for supercapacitor applications, particularly in applications where cost-effectiveness and ease of production are essential.

Oxygen evolution reaction (OER). The OER activity of Fe_3O_4 and its carbon-based composites was assessed *via* LSV, as illustrated in Fig. 10. No significant current response was detected in the negative potential region, indicating the absence of the hydrogen evolution reaction (HER) under the specified conditions. A notable increase in anodic current was observed upon raising the applied potential above approximately 0.55 V *vs.* Ag/AgCl, thereby affirming the initiation of the OER and demonstrating the electrocatalytic efficacy of the examined materials (Fig. 10a).

Varied electrochemical characteristics were noted among the samples. Pristine Fe_3O_4 and Fe_3O_4@CNT exhibited significant anodic behavior, with a peak at approximately 0.46 V *vs.* Ag/AgCl. Conversely, Fe_3O_4@CF and Fe_3O_4@G exhibited wider anodic responses with a negative potential shift to approximately 0.43 V, signifying altered surface kinetics and improved charge-transfer properties resulting from carbon incorporation (Fig. 10a).

The LSV curves were transformed to the reversible hydrogen electrode (RHE) scale for precise comparison (Fig. 10c). The OER overpotentials were subsequently assessed at a constant current density, and the results are shown in Fig. 10d. The determined overpotential values were 380 mV for Fe_3O_4, 360 mV for Fe_3O_4@G, 390 mV for Fe_3O_4@CF, and 400 mV for Fe_3O_4@CNT (Fig. 10a).

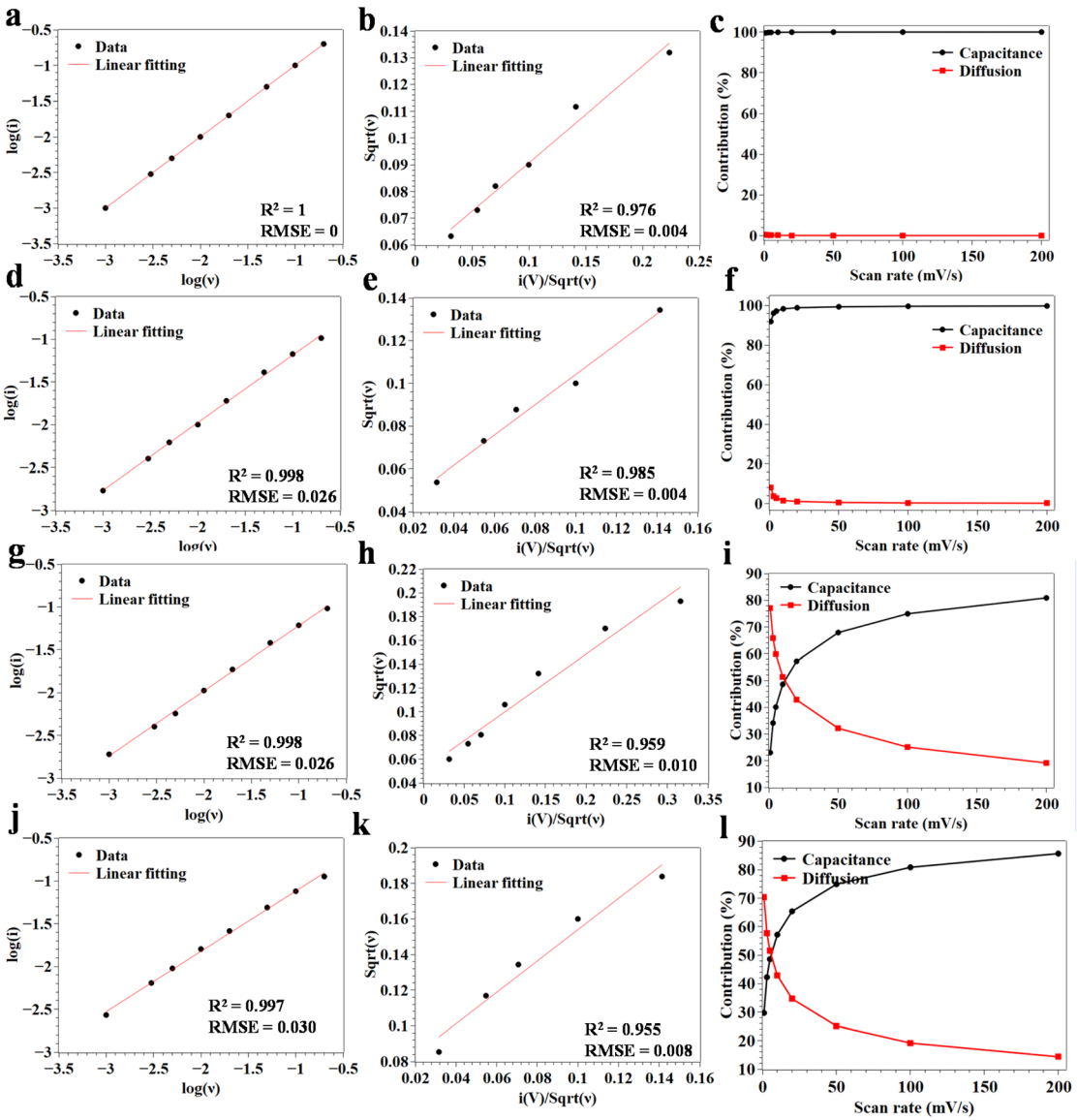

Fig. 9 *b*-Value and Dunn methods for (a–c) Fe_3O_4, (d–f) Fe_3O_4@G, (g–i) Fe_3O_4@CF, and (j–l) Fe_3O_4@CNT.

Among the tested catalysts, Fe_3O_4@G exhibited the lowest overpotential, indicating improved OER kinetics driven by enhanced electrical conductivity and synergistic interactions between Fe_3O_4 and the graphite support. While Fe_3O_4@CF exhibited exceptional performance in supercapacitor applications, its OER activity was lower, underscoring the unique structure–property interactions that govern energy storage and electrocatalytic behavior.

Table 2 compares the overpotentials for OER of Fe_3O_4-based electrocatalysts reported in the literature. The Fe_3O_4 composites produced in this study exhibit low, competitive overpotentials (360–400 mV), indicating efficient OER activity despite their straightforward synthesis and lack of noble metals or intricate structures. In contrast to Fe_3O_4/N-doped carbon foam (Fe_3O_4/N-CF), which demonstrated improved OER performance under an external magnetic field with a bifunctional potential differential of 700 mV,[65] the current materials exhibit similar overpotential values in the absence of a magnetic field. Au/Fe_3O_4 electrocatalysts exhibited a significant decrease in overpotential due to enhanced interfacial charge transfer; however, their efficacy depended on the inclusion of noble metals and supplementary fabrication steps.[66] Core–shell Fe_3O_4@$CoFe_2O_4$ systems exhibited OER activity that was significantly influenced by the catalyst layer thickness, with high overpotentials resulting from charge-transport resistance at higher loadings.[67] Coral-like Fe_3O_4 nanostructures exhibited a remarkably low overpotential of 234 mV at 10 mA/cm^2, owing to optimal shape and calcination conditions, necessitating temperature control during synthesis.[68] The Fe_3O_4 and Fe_3O_4/carbon composites presented herein exhibit competitive OER overpotentials compared to previously reported Fe_3O_4-based catalysts, while offering the advantages of simpler preparation, reduced cost, and enhanced structural stability, underscoring their viability as practical OER electrocatalysts.

Table 1 Summary of different Fe_3O_4 reported for supercapacitors

Materials	Synthesis methods	Conditions	Electrolytes	Specific capacitance	Recyclability	Ref.
AE-AC	Extraction carbonization	500 °C for 2 h	1 M H_2SO_4	119.97 F/g 0.05 A/g	91.34% after 1000 cycles at 0.1 A/g	40
AE-AC-doped Fe_3O_4	Precipitation freeze-drying	30 min at 90 °C for 30 min 1000 rpm for 6 h freeze-drying		205.86 F/g at 0.05 A/g	88.20% after 1000 cycles at 0.2 A/g	
ISCC-Fe_3O_4	Carbonization	Argon atmosphere at 1200 °C	1 M Na_2SO_4	150 F/g at 1.5 A/g		42
Fe_3O_4@rGO	Hummer's method reduction hydrolysis	Reducing GO in NaOH solution at 80 °C heating the mixture to 80 °C	1 LiOH	326 F/g at 0.5 A/g	95% after 1000 cycles at 2 A/g	43
FeCHNPs	Electrospray heating carbonization	Stirring at 70 8C for 4 h dried at 60 °C for 12 h vaporized pyrrole for 5 min at room carbonized at 400 °C for 1 h in an argon	1 M Na_2SO_3	455 F/g at 1 A/g	91% after 3000 cycles at 1 A/g	45
PPy NPs	Polymerization	$FeCl_3$-catalysis		105 F/g at 1 A/g		
Fe_3O_4@CF	Precipitation ultrasonication	60 °C for 30 min	6 M KOH	106 F/g at 1 A/g	100% after 5000 cycles at 10 A/g	This study

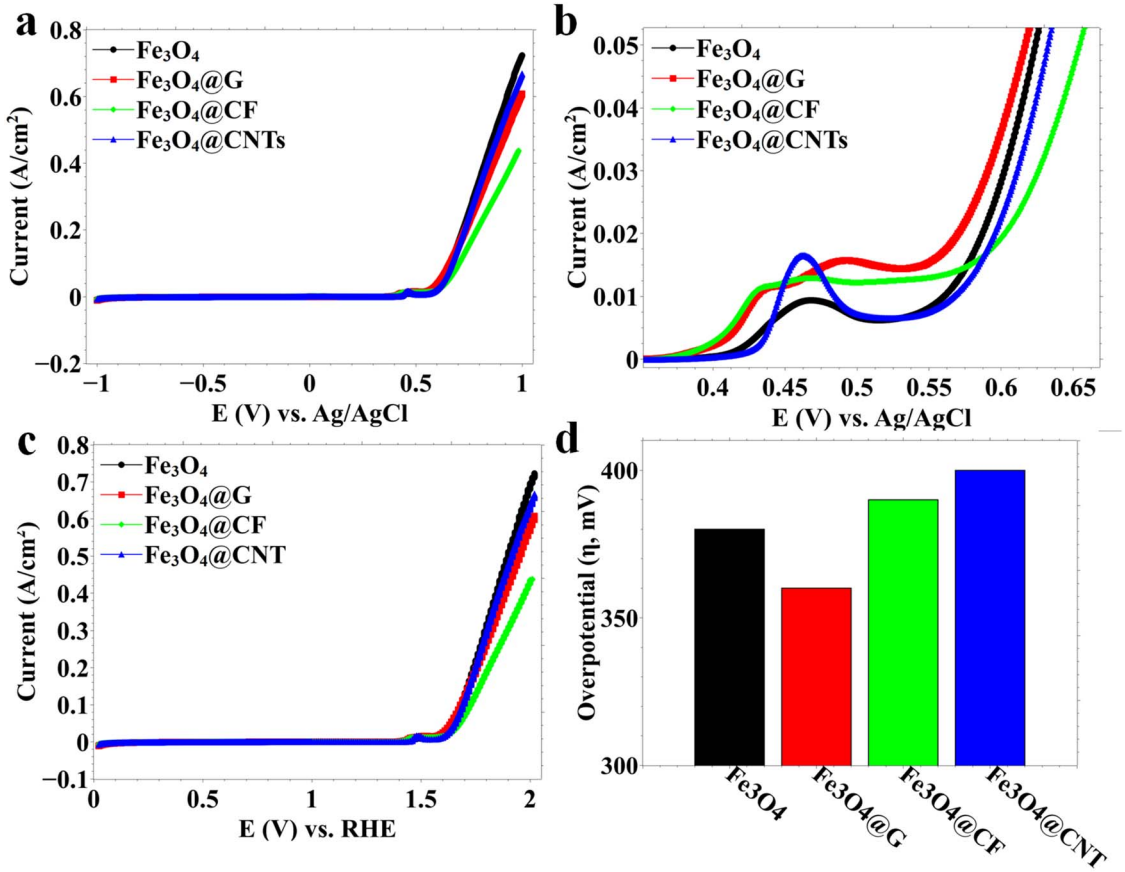

Fig. 10 (a–c) LSV curves for (a and b) *vs.* Ag/AgCl and (c) *vs.* RHE, and (d) overpotential for different materials.

Table 2 Summary of different Fe_3O_4 reported for OER

Materials	Synthesis methods	Conditions	Electrolytes	Overpotential	Ref.
Fe_3O_4/N-CF	NaCl-assisted method carbonization	750 °C for 2 h	0.1 M KOH	700 mV@10 mA/cm^2	65
Fe_3O_4/Au	Hydrothermal electrochemical deposition	200 °C for 12 h −0.9 V (*vs.* SCE) for 3 min	0.1 M KOH	640 mV@10 mA/cm^2	66
Fe_3O_4@$CoFe_2O_4$	Seed-mediated growth, thermal decomposition	Reflux for 15 min 100 °C for 30 min reflux for 2 h	0.1 M NaOH	150–250 mV@10 mA/cm^2	67
Fe_3O_4	Template-assisted dipping adsorbing-calcining	Heating at 600 °C for 2 h	1.0 M NaOH	234 mV@10 mA/cm^2	68
Fe_3O_4@G	Precipitation ultrasonication	Heating at 60 °C for 30 min	6 M KOH	360 mV@20 mA/cm^2	This study

Conclusions

In conclusion, Fe_3O_4 nanoparticles and their composites with graphite, carbon fibers, and carbon nanotubes were effectively produced using a straightforward ultrasonic-assisted co-precipitation technique. Structural and morphological investigations verified the retention of magnetite crystallinity and nanoscale particle dimensions following composite production. Electrochemical analyses demonstrated that carbon insertion markedly improved charge-storage characteristics, yielding hybrid supercapacitive performance that combines electric double-layer capacitance with Fe^{2+}/Fe^{3+} redox activity. Among the examined materials, Fe_3O_4@CF demonstrated exceptional electrochemical performance, achieving a specific capacitance of 106 F/g at 1 A/g and exhibiting notable cycling stability over 5000 cycles. Furthermore, Fe_3O_4 and its composites exhibited notable oxygen evolution reaction activity with low overpotentials, affirming their viability as economical OER electrocatalysts. The findings underscore the efficacy of straightforward carbon–magnetite integration techniques for creating multifunctional materials suitable for energy storage and water-oxidation applications.

Author contributions

Hani Nasser Abdelhamid: writing – review & editing, writing – original draft, visualization, validation, supervision, software, resources, project administration, methodology, investigation, formal analysis, data curation, conceptualization. Walid M. Daoush: writing – review & editing, resources, data curation, project administration, methodology, investigation, funding acquisition, formal analysis, conceptualization. Faisal Saleh Alshebil: methodology, investigation, formal analysis.

Conflicts of interest

The authors declare that they have no known competing financial interests or personal relationships that could have influenced the work reported in this paper.

Data availability

The data supporting the manuscript can be found within the manuscript, as well as in the following repository for raw data; Abdelhamid, Hani Nasser; Alshebil, Faisal Saleh; Daoush, Walid M. (2026), "RawData", Mendeley Data, V1, doi: https://doi.org/10.17632/v247syhsgw.1.

Acknowledgements

This work was supported and funded by the Deanship of Scientific Research at Imam Mohammad Ibn Saud Islamic University (IMSIU) (grant number IMSIU-DDRSP2603).

References

1 X. Ding, L. Duan, N. Zheng, U. Desideri, Y. Zhou, Q. Wang, *et al.*, A systematic review on liquid air energy storage system, *Renew. Sustain. Energy Rev.*, 2025, **210**, 115164, DOI: 10.1016/j.rser.2024.115164.
2 S. Mandal, A. B. Mendhe, H. M. Rakhade, N. S. Barse, M. Roy, P. Rosaiah, *et al.*, Recent advancement and design in supercapacitor hybrid electrode materials: Bridging the gap between energy and power density, *Chem. Eng. J. Adv.*, 2025, **21**, 100690, DOI: 10.1016/j.ceja.2024.100690.
3 M. Domínguez, A. Fernández-Cardador, A. Fernández-Rodríguez, A. P. Cucala, R. R. Pecharromán, P. Urosa Sánchez, *et al.*, Review on the use of energy storage systems in railway applications, *Renew. Sustain. Energy Rev.*, 2025, **207**, 114904, DOI: 10.1016/j.rser.2024.114904.
4 N. Raza, K. Aziz, M. S. Javed, R. Tariq, N. Kanwal, W. Raza, *et al.*, Advancements in separator design for supercapacitor technology: A review of characteristics, manufacturing processes, limitations, and emerging trends, *J. Energy Storage*, 2025, **111**, 115328, DOI: 10.1016/j.est.2025.115328.
5 S. Seenivasan, S. Adhikari, A. T. Sivagurunathan and D.-H. Kim, Supercapatteries: unlocking the potential of battery-supercapacitor fusion, *Energy Environ. Sci.*, 2025, **18**, 1054–1095, DOI: 10.1039/D4EE04348K.
6 P. M. Anjana and T. M. Aminabhavi, Supercapattery: Energy storage devices combining functionalities of battery electrodes and supercapacitor electrodes, *J. Energy Storage*, 2025, **134**, 118265, DOI: 10.1016/j.est.2025.118265.
7 D. M. Teffu, K. Makgopa, T. R. Somo, M. S. Ratsoma, S. Honey, E. Makhado, *et al.*, Metal and covalent organic frameworks (MOFs and COFs): A comprehensive overview of their synthesis, characterization and enhanced

supercapacitor performance, *Coord. Chem. Rev.*, 2025, **540**, 216798, DOI: 10.1016/j.ccr.2025.216798.

8 Z. H. Hashem, L. H. Abdel-Rahman, S. Gómez-Ruiz and H. N. Abdelhamid, A Multifunctional Nickel-Based Metal–Organic Framework (MOF) for Hydrogen Production, Supercapacitors, and Electrocatalysis, *Catalysts*, 2026, **16**, 283, DOI: 10.3390/catal16030283.

9 H. N. Abdelhamid, Metal-Organic Framework (UiO-66-NH_2) as a Dual-Functional Material for Photo-Assisted Nitroarene Reduction and Supercapacitor Applications, *Catalysts*, 2026, **16**, 172, DOI: 10.3390/catal16020172.

10 A. Singh, N. Lalotra, S. S. Shah, M. ud D. Rather, E. A. Lopez-Maldonado, K. Pathania, *et al.*, A Comprehensive Review on the Synthesis and Properties of MXenes for Supercapacitor Applications, *ACS Appl. Energy Mater.*, 2025, **8**, 4884–4914, DOI: 10.1021/acsaem.4c03194.

11 L. Wang, X. Gao, D. Wang, H. Shang, Y. Zhao and B. Zhang, Nickel-carbon composites toward supercapacitor and self-charging systems: A review, *Fuel*, 2025, **381**, 133639, DOI: 10.1016/j.fuel.2024.133639.

12 H. N. Abdelhamid and W. M. Daoush, Carbon nanomaterials enhance copper electrochemical performance as supercapacitors, *Synth. Met.*, 2026, **319**, 118148, DOI: 10.1016/j.synthmet.2026.118148.

13 H. N. Abdelhamid and W. M. Daoush, Copper-loaded carbon fiber for supercapacitors and oxygen evolution reaction, *Diam. Relat. Mater.*, 2026, **165**, 113546, DOI: 10.1016/j.diamond.2026.113546.

14 M. B. Askari, P. Salarizadeh, M. T. Tourchi Moghadam, S. Azizi and M. H. Ramezan zadeh, Binary transition metal oxide/carbon compounds-based electrode materials for supercapacitor application: A comprehensive review, *J. Alloys Compd.*, 2025, **1027**, 180573, DOI: 10.1016/j.jallcom.2025.180573.

15 V. A. Kadam, V. L. Patil, S. H. Mujawar, A. P. Torane and L. D. Kadam, Recent advances of spinel CuCo2O4 in different Structural dimensions (0D-3D) for an electrochemical supercapacitor device: A short research review, *J. Alloys Compd.*, 2025, **1010**, 177581, DOI: 10.1016/j.jallcom.2024.177581.

16 M. Saxena, S. A. Patil, S. Reza, A. Das, R. Thapa and P. K. Misra, Single-Crystalline Fe2O3 on Reduced Graphene Oxide as an Anode Material for All-Solid-State Supercapacitors, *ACS Appl. Nano Mater.*, 2025, **8**, 8948–8962, DOI: 10.1021/acsanm.5c01048.

17 R. Kumar, A. Soam, R. Hossain, I. Mansuri and V. Sahajwalla, Carbon coated iron oxide (CC-IO) as high performance electrode material for supercapacitor applications, *J. Energy Storage*, 2020, **32**, 101737, DOI: 10.1016/j.est.2020.101737.

18 R. Kumar, A. Soam and V. Sahajwalla, Carbon coated cobalt oxide (CC-Co_3O_4) as electrode material for supercapacitor applications, *Mater. Adv.*, 2021, **2**, 2918–2923, DOI: 10.1039/D1MA00120E.

19 R. Kumar, B. K. Singh, A. Soam, S. Parida, V. Sahajwalla and P. Bhargava, In situ carbon-supported titanium dioxide (ICS-TiO_2) as an electrode material for high performance supercapacitors, *Nanoscale Adv.*, 2020, **2**, 2376–2386, DOI: 10.1039/D0NA00014K.

20 R. Kumar, A. Soam and V. Sahajwalla, Sucrose-derived carbon-coated nickel oxide (SDCC-NiO) as an electrode material for supercapacitor applications, *Mater. Adv.*, 2020, **1**, 609–616, DOI: 10.1039/D0MA00323A.

21 Z. M. Hassan, F. M. Elantabli, S. G. Mohamed and H. N. Abdelhamid, Metal-organic frameworks (MOFs)-derived zinc selenide and cobalt selenide for asymmetric supercapacitors, *J. Energy Storage*, 2026, **141**, 119311, DOI: 10.1016/j.est.2025.119311.

22 N. Kumar, R. Aepuru, S.-Y. Lee and S.-J. Park, Recent advances in phosphorene: A promising material for supercapacitor applications, *Mater. Sci. Eng., R*, 2025, **163**, 100932, DOI: 10.1016/j.mser.2025.100932.

23 A. A. Bhoite, V. A. Sawant and N. L. Tarwal, A brief review of Nickel cobaltite nanostructures and its composites for supercapacitor application, *J. Alloys Compd.*, 2025, **1010**, 177657, DOI: 10.1016/j.jallcom.2024.177657.

24 K. Kumar, U. Tyagi, S. Sirohi, R. Kumar, S. Kumar Maity, Nikita, S. Singh and G. Kumar, A critical review on nanostructure-doped carbonized biomass: A new Era in sustainable supercapacitor technology, *Fuel*, 2025, **381**, 133707, DOI: 10.1016/j.fuel.2024.133707.

25 J. Feng, Q. Zhu, Q. Le, W. Zhu, B. Song, Z. Zhang, *et al.*, Source and performance of waste-derived porous carbon material as supercapacitor: Biomass, sludge and plastic waste as precursors, *Renew. Sustain. Energy Rev.*, 2025, **211**, 115178, DOI: 10.1016/j.rser.2024.115178.

26 P. K. Ray and K. Parida, Achievements, challenges, and stability of layer double hydroxide and carbon nanotube hybrid electrode materials for clean and sustainable energy storage supercapacitor application: an extensive review, *Mater. Adv.*, 2025, **6**, 84–116, DOI: 10.1039/d4ma00772g.

27 S. B. Srinivasan, S. Devendiran, K. V. Savunthari, P. Arumugam and S. Mukerjee, Insights into multifarious heteroatom-doped/enriched carbon-based materials and their composites: Synthesis and Supercapacitor applications – A crucial review, *Prog. Mater. Sci.*, 2025, **153**, 101470, DOI: 10.1016/j.pmatsci.2025.101470.

28 G. Hasanova, S. Omarova, N. Abdullayeva, R. Khalilov, A. Mammadova, M. F. Baran, *et al.*, Bioinspired silver nanoparticles from Artemisia lerchiana as durable electrodes for next-generation supercapacitors, *Phys. Chem. Chem. Phys.*, 2026, **28**, 8706–8714, DOI: 10.1039/d5cp05057j.

29 M. F. Baran, E. Huseynov, A. Eftekhari, A. Levent, E. Ertaş, T. Kavetskyy, *et al.*, High-Capacitance Gold Nanoparticles from Rhus coriaria: Green Synthesis, Characterization and Electrochemical Evaluation for Supercapacitor Technologies, *Micromachines*, 2026, **17**, 82, DOI: 10.3390/mi17010082.

30 K. Wu, J.-P. Wang, N. A. Natekar, S. Ciannella, C. González-Fernández, J. Gomez-Pastora, *et al.*, Roadmap on magnetic nanoparticles in nanomedicine, *Nanotechnology*, 2025, **36**, 042003, DOI: 10.1088/1361-6528/ad8626.

31 Y. Yu, C. Zhang, X. Yang, L. Sun and F. Bian, Microfluidic Synthesis of Magnetic Nanoparticles for Biomedical

Applications, *Small Methods*, 2025, **9**(4), 2401220, DOI: 10.1002/smtd.202401220.

32 W. Graham, M. Torbett-Dougherty, A. Islam, S. Soleimani, T. A. Bruce-Tagoe and J. A. Johnson, Magnetic Nanoparticles and Drug Delivery Systems for Anti-Cancer Applications: A Review, *Nanomaterials*, 2025, **15**, 285, DOI: 10.3390/nano15040285.

33 M. S. Khan, G. Gupta, M. Ghazwani, U. Hani, K. W. Goh and P. Kesharwani, Translational Insights into Stimuli-Responsive Magnetic Nanoparticles for Breast Cancer Treatment, *Mol. Pharm.*, 2025, **22**, 4494–4511, DOI: 10.1021/acs.molpharmaceut.5c00473.

34 A. Shakeri-Zadeh and J. W. M. Bulte, Imaging-guided precision hyperthermia with magnetic nanoparticles, *Nat. Rev. Bioeng.*, 2024, **3**, 245–260, DOI: 10.1038/s44222-024-00257-3.

35 S. Rohith, K. Radhakrishnan, A. Dinesh, S. Sakthivel, R. P. Patil, L. Gnanasekaran, *et al.*, Review on the Recent Developments in Magnetic Nanocomposites for Energy Storage Applications, *Semiconductors*, 2025, **59**, 91–114, DOI: 10.1134/S106378262460219X.

36 S. A. Al Kiey, F. K. Algethami and H. N. Abdelhamid, Ferric Oxide@Carbon-Derived from Fe-MOF for Supercapacitor, *Arabian J. Sci. Eng.*, 2025, DOI: 10.1007/s13369-025-10689-7.

37 J. Belisario and J. Thomas, Enhanced Performance in Batteries and Supercapacitors Using Magnetic Stimuli, *Small*, 2026, **22**(3), e06533, DOI: 10.1002/smll.202506533.

38 M. F. Ahmer, Q. Ullah and M. K. Uddin, Magnetic metal oxide assisted conducting polymer nanocomposites as eco-friendly electrode materials for supercapacitor applications: a review, *J. Polym. Eng.*, 2025, **45**, 1–41, DOI: 10.1515/polyeng-2024-0101.

39 M. Shakoor, G. Ali, K. T. Kubra, A. Butt, F. Iqbal, S. Zehra, *et al.*, Electrochemical investigations of Fe_3O_4/ZnO/carbon ternary composite derived from bimetallic metal-organic framework for supercapacitor applications, *Inorg. Chem. Commun.*, 2025, **182**, 115586, DOI: 10.1016/j.inoche.2025.115586.

40 K. S. Aslan, E. Ertaş, M. F. Baran, A. Levent, Ş. Tümür, A. Eftekhari, *et al.*, Enhanced Electrochemical Performance of Supercapacitors Using Fe_3O_4 -Doped Biomass-Derived Activated Carbon Electrodes, *Electrochem. Sci. Adv.*, 2026, **6**(1), e70014, DOI: 10.1002/elsa.70014.

41 A. B. Pandhare, S. V. Mulik, B. E. Keshta, P. N. Nikam, M. Ayyar, S. Santhoshkumar, *et al.*, Energy storage studies of a novel green route synthesized high-performance supercapacitor based on Fe_3O_4, *J. Mater. Sci. Mater. Electron.*, 2026, **37**, 21, DOI: 10.1007/s10854-025-16407-1.

42 R. Kumar, R. K. Nekouei and V. Sahajwalla, In-situ carbon-coated iron oxide (ISCC-Fe3O4) as an efficient electrode material for supercapacitor applications, *Ceram. Int.*, 2025, **51**, 12312–12320, DOI: 10.1016/j.ceramint.2025.01.071.

43 Q. Qu, S. Yang and X. Feng, 2D Sandwich-like Sheets of Iron Oxide Grown on Graphene as High Energy Anode Material for Supercapacitors, *Adv. Mater.*, 2011, **23**, 5574–5580, DOI: 10.1002/adma.201103042.

44 B. C. Yallur, M. P. Rao, M. Harshitha, D. Basrur, P. H. Umesh, V. Kamat, *et al.*, Recent Advances in Graphene-Based Metal Oxide Composites for Supercapacitors: A Comprehensive Review, *Adv. Sustain. Syst.*, 2025, **9**(8), 2500121, DOI: 10.1002/adsu.202500121.

45 J. S. Lee, D. H. Shin, J. Jun, C. Lee and J. Jang, Fe_3O_4/Carbon Hybrid Nanoparticle Electrodes for High-Capacity Electrochemical Capacitors, *ChemSusChem*, 2014, **7**, 1676–1683, DOI: 10.1002/cssc.201301188.

46 H. N. Abdelhamid and S. A. Salim, Ferric metal-organic frameworks (MOFs)-based electrospinning fibers for supercapacitors, *React. Funct. Polym.*, 2025, **217**, 106466, DOI: 10.1016/j.reactfunctpolym.2025.106466.

47 H. N. Abdelhamid, A review on hydrogen generation from the hydrolysis of sodium borohydride, *Int. J. Hydrogen Energy*, 2021, **46**, 726–765, DOI: 10.1016/j.ijhydene.2020.09.186.

48 H. N. Abdelhamid and H. M. El-Bery, Two-dimensional metal-organic frameworks for photocatalytic water splitting over TiO2, *Inorg. Chem. Commun.*, 2025, **180**, 115044, DOI: 10.1016/j.inoche.2025.115044.

49 H. N. Abdelhamid, A. B. A. Abdellatif and H. M. El-Bery, Hydrogen production using noble metal-free metal-organic frameworks (MOFs)-derived CuO@C/TiO_2, *Chem. Eng. J.*, 2025, **514**, 163343, DOI: 10.1016/j.cej.2025.163343.

50 R. Hu, C. Wen, Z. Ye, Y. Qi, B. Zhang, K. Kang, *et al.*, A comprehensive review of flow channel designs and optimizations for water electrolysis technology, *Appl. Energy*, 2025, **400**, 126643, DOI: 10.1016/j.apenergy.2025.126643.

51 H. N. Abdelhamid, Ni/Cu Metal-Organic Frameworks (MOFs)-derived NiO/CuO@C for Supercapacitors and Oxygen Evolution Reaction, *Surf. Interfaces*, 2025, 107923, DOI: 10.1016/j.surfin.2025.107923.

52 R. A. Alsaiari, I. Gomaa and H. N. Abdelhamid, Eco-Engineered Co_3O_4/CoO/C Nanohybrid for Supercapacitors and Efficient Water Splitting, *Arabian J. Sci. Eng.*, 2025, DOI: 10.1007/s13369-025-10606-y.

53 A. Z. Alhakemy, M. H. Elsayed, F. K. Algethami and H. N. Abdelhamid, Metal-organic framework (MOF)-derived bimetallic (Ni, Cu) Oxide@C electrocatalyst for oxygen evolution reaction, *Int. J. Hydrogen Energy*, 2025, **115**, 289–298, DOI: 10.1016/j.ijhydene.2025.01.206.

54 K. Lellala, Microwave-Assisted Facile Hydrothermal Synthesis of Fe_3O_4 –GO Nanocomposites for the Efficient Bifunctional Electrocatalytic Activity of OER/ORR, *Energy Fuels*, 2021, **35**, 8263–8274, DOI: 10.1021/acs.energyfuels.0c04411.

55 M. Müllner, M. Riva, F. Kraushofer, M. Schmid, G. S. Parkinson, S. F. L. Mertens, *et al.*, Stability and Catalytic Performance of Reconstructed Fe_3O_4 (001) and Fe_3O_4 (110) Surfaces during Oxygen Evolution Reaction, *J. Phys. Chem. C*, 2019, **123**, 8304–8311, DOI: 10.1021/acs.jpcc.8b08733.

56 F. Jafari and F. R. Rahsepar, V_2O_5 –Fe_3O_4/rGO Ternary Nanocomposite with Dual Applications as a Dye Degradation Photocatalyst and OER Electrocatalyst, *ACS*

Omega, 2023, **8**, 35427–35439, DOI: 10.1021/acsomega.3c06094.

57 D. Grumelli, T. Wiegmann, S. Barja, F. Reikowski, F. Maroun, P. Allongue, *et al.*, Electrochemical Stability of the Reconstructed Fe_3O_4 (001) Surface, *Angew. Chem., Int. Ed.*, 2020, **59**, 21904–21908, DOI: 10.1002/anie.202008785.

58 E. Bianchetti, D. Perilli and C. Di Valentin, Improving the Oxygen Evolution Reaction on Fe 3 O 4 (001) with Single-Atom Catalysts, *ACS Catal.*, 2023, **13**, 4811–4823, DOI: 10.1021/acscatal.3c00337.

59 E. Soltani, M. B. Gholivand, A. A. Taherpour, M. Norouzibazaz and M. Mirzaei, Construction of aspartic acid -Fe MOF derived Fe_3O_4@NC implanted on rGO as a remarkably efficient catalyst for the oxygen and hydrogen evolution reactions, *Fuel*, 2025, **395**, 135249, DOI: 10.1016/j.fuel.2025.135249.

60 A. Huang, R. Xu, D. Zhao, X. Gao and Z. Chen, Self-driven coupling field in Fe3O4@NiFe-LDH/MnCO3 heterojunction for electrocatalytic water oxidation at high current densities, *Chem. Eng. J.*, 2025, **521**, 166883, DOI: 10.1016/j.cej.2025.166883.

61 R. Barath, S. Vadivel, S. Sarmila, P. Sujita, N. Murugan and Y. A. Kim, Core-Shell Co3Fe7/Fe3O4 electrocatalyst *via* MOF Engineering: Unlocking superior oxygen evolution activity for water splitting, *Mater. Lett.*, 2025, **399**, 139056, DOI: 10.1016/j.matlet.2025.139056.

62 X.-Y. Jia, Z. Chen, M.-D. Liu, Y. Chang, S. Zhang, F. Zeng, *et al.*, Preparation and properties of Fe3O4-based dimensionally stable anodes derived by high-temperature sintering for water electrolysis, *Ceram. Int.*, 2025, **51**, 59730–59736, DOI: 10.1016/j.ceramint.2025.10.197.

63 I. Makarchuk, B. Rotonnelli, L. Royer, S. Hettler, J.-J. Gallet, F. Bournel, *et al.*, Effect of Shell Thickness on the Oxygen Evolution Activity of Core@shell Fe_3O_4@$CoFe_2O_4$ Nanoparticles, *Chem. Mater.*, 2025, **37**, 833–844, DOI: 10.1021/acs.chemmater.4c01784.

64 M. FAIZAN and H. ÇELİKTEN, Mitigation of Ozone (O_3) Effects and Enhanced Air-Purifying Capacity of Plants by Carbon-Based Nanomaterials, *MAS J. Appl. Sci.*, **1**, 168–180, DOI: 10.5281/zenodo.19127754.

65 K. Kakaei, Y. Aykut and A. Bayrakçeken, Facile synthesis multifaceted Fe3O4 based on N-Doped Porous Carbon frameworks for ORR/OER and study of an external magnetic field, *Electrochim. Acta*, 2025, **541**, 147319, DOI: 10.1016/j.electacta.2025.147319.

66 W. Zhang, H. Guan, Y. Hu, W. Wang, X. Yang and C. Kuang, Enhancing catalytic activity of Fe3O4 for electrochemical water oxidation *via* the coupling of OER-inert Au, *Int. J. Hydrogen Energy*, 2022, **47**, 22731–22737, DOI: 10.1016/j.ijhydene.2022.05.100.

67 L. Royer, J. Guehl, M. Zilbermann, T. Dintzer, C. Leuvrey, B. P. Pichon, *et al.*, Influence of the catalyst layer thickness on the determination of the OER activity of Fe3O4@CoFe2O4 core-shell nanoparticles, *Electrochim. Acta*, 2023, **446**, 141981, DOI: 10.1016/j.electacta.2023.141981.

68 M. Wei, Y. Han, Y. Liu, B. Su, H. Yang and Z. Lei, Green preparation of Fe3O4 coral-like nanomaterials with outstanding magnetic and OER properties, *J. Alloys Compd.*, 2020, **831**, 154702, DOI: 10.1016/j.jallcom.2020.154702.